Geophys. J. Int. (2003) **152,** 171–184

Three-dimensional seismic refraction tomography of the crustal structure at the ION site on the Ninetyeast Ridge, Indian Ocean

Vera Schlindwein,[1] Christian Bönnemann,[1] Christian Reichert,[1]
Ingo Grevemeyer[2] and Ernst Flueh[3]

[1] *Federal Institute for Geosciences and Natural Resources, Hannover, Germany. E-mail: V.Schlindwein@bgr.de*
[2] *FB Geowissenschaften, University of Bremen, Bremen, Germany*
[3] *GEOMAR Research Centre for Marine Geosciences, Kiel, Germany*

Accepted 2002 July 20. Received 2002 July 11; in original form 2002 February 27

SUMMARY

We have performed a 3-D seismic refraction tomography of a 48 × 48 km^2 area surrounding ODP site 757, which is planned to host an International Ocean Network (ION) permanent seismological observatory, called the Ninetyeast Ridge Observatory (NERO). The study area is located in the southern part of the Ninetyeast Ridge, the trail left by the Kerguelen hotspot on the Indian plate. The GEOMAR Research Centre for Marine Geosciences and the Federal Institute for Geosciences and Natural Resources acquired 18 wide-angle profiles recorded by 23 ocean bottom hydrophones during cruise SO131 of *R/V Sonne* in spring 1998. We apply a first arrival traveltime tomography technique using regularized inversion to recover the 3-D velocity structure relative to a 1-D background model that was constructed from *a priori* information and averaged traveltime data. The final velocity model revealed the crustal structure down to approximately 8 km depth. Resolution tests showed that structures with approximately 6 km horizontal extent can reliably be resolved down to that depth. The survey imaged the extrusive layer of the upper crust of the Ninetyeast Ridge, which varies in thickness between 3 and 4 km. A high-velocity anomaly coinciding with a positive magnetic anomaly represents a volcanic centre from which crust in this area is thought to have formed. A pronounced low-velocity anomaly is located underneath a thick sedimentary cover in a bathymetric depression. However, poor ray coverage of the uppermost kilometre of the crust in this area resulted in smearing of the shallow structure to a larger depth. Tests explicitly including the shallow low-velocity layer confirmed the existence of the deeper structure. The heterogeneity of the upper crust as observed by our study will have consequences for the waveforms of earthquake signals to be recorded by the future seismic observatory.

Key words: hotspot, Ninetyeast Ridge, oceanic crust, seismic refraction, tomography, volcanic structure.

INTRODUCTION

In spring 1998, the Research Centre for Marine Geosciences (GEOMAR) and the Federal Institute for Geosciences and Natural Resources (BGR) undertook an intensive seismic survey of the Ninetyeast Ridge during *R/V Sonne* cruise SO131 (Flueh & Reichert 1998; Flueh *et al.* 1999). The project, called SINUS (seismic investigations at the Ninetyeast Ridge Observatory (NERO) using *Sonne* and *Joides Resolution* during ODP Leg 179) aimed to study the crust and upper mantle of the Ninetyeast Ridge. ODP site 757 was chosen to host the first International Ocean Network (ION) permanent seismic observatory, which has become feasible because of advantages in technology (Montagner *et al.* 1994). In order to reliably interpret earthquake signals to be recorded by the future observatory, detailed knowledge of the lateral variations of the seismic properties of the crust in the vicinity of the observatory is necessary.

A 3-D seismic survey using ocean bottom hydrophones (OBHs) around ODP site 757 was designed to reveal the small-scale structure of the Ninetyeast Ridge volcanic edifice. The survey complements a 550 km long seismic refraction profile investigating the architecture of the crust and upper mantle (Grevemeyer *et al.* 2001) and high-resolution seismic and multibeam sonar studies of the immediate vicinity of the NERO site (Grevemeyer *et al.* 1999; Kopf *et al.* 2001). A heterogeneous upper crustal architecture, comprising an extrusive layer formed at discrete volcanic centres at sea level (Peirce *et al.* 1989), is expected and can only be captured insufficiently by a 2-D study along selected but not representative profiles. A 3-D refraction

survey was therefore conducted with seismic rays travelling not only along profiles but between all shots and receivers sampling the crust extensively in three dimensions. By combining the results of all studies a comprehensive model of the lateral variability of the upper crust around the NERO site will be compiled.

TECTONIC SETTING

The Ninetyeast Ridge is a major aseismic ridge that extends nearly meridionally for approximately 5000 km from the Bay of Bengal in the north to Broken Ridge in the south (Fig. 1). It is elevated

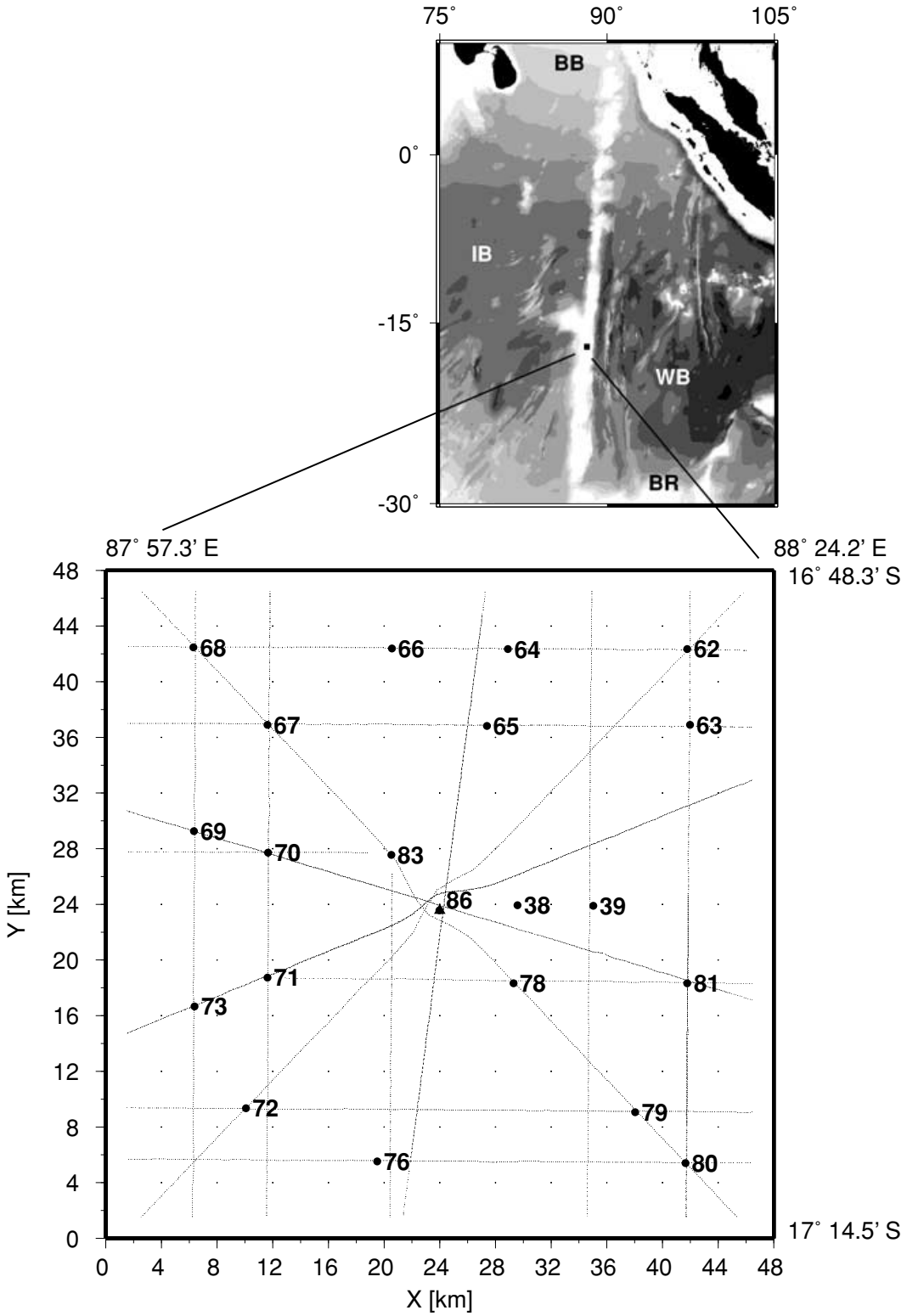

Figure 1. Location of the study area in the eastern Indian ocean (relief, ETOPO5; BB, Bay of Bengal; IB, Indian Basin; WB, Wharton Basin; BR, Broken Ridge) and experimental design of the 3-D refraction seismic survey of the NERO site (triangle in the lower figure). Thin lines show seismic profile lines with airgun shots with roughly 150 m shot intervals. Solid circles mark OBH sites and numbers.

approximately 2000 m above the adjacent ocean basins (the Indian Basin to the west and the Wharton Basin to the east). Deep Sea Drilling Project (DSDP) legs 22 and 26 and Ocean Drilling Programme (ODP) leg 121 and related scientific investigations revealed the origin of the Ninetyeast Ridge (e.g. Peirce 1978; Peirce *et al.* 1989; Duncan 1991; Royer *et al.* 1991). It is considered to represent the track left by the Kerguelen hotspot on the rapidly northward-drifting Indian plate. Consequently, the ages of the ridge increase northwards from 38 Myr near Broken Ridge to approximately 80–82 Myr in the Bay of Bengal. The ridge can be divided into three units representing different stages of tectonic evolution: the segment north of 5°S is formed by intraplate volcanism, whereas the more voluminous middle and southern segments of the ridge were extruded along a transform plate boundary (Royer *et al.* 1991). The study area is located in this southern segment. The volcanic edifice of the Ninetyeast Ridge in this area probably formed by eruptions from discrete volcanic centres situated at or just below sea level (Peirce *et al.* 1989). Rapid subsidence accompanied the formation of the ridge such that little erosional material accumulated and volcanic cones of late-stage volcanism remained intact (e.g. Grevemeyer & Flueh 2000). The present study aims to understand the small-scale structure of the upper 5–7 km of the crust, which is not imaged by shallow-seismic reflection and refraction studies nor resolved by deep crustal studies.

DATA AND DATA PREPARATION

Definition of 3-D tomography area

The survey area of the SINUS project extends between 16°45′S and 17°20′S, and 87°50′E and 88°30′E (Fig. 1). For the tomographic inversion of the wide-angle seismic data, the geographical coordinates of all shot and receiver positions were transformed into rectangular coordinates using the Universal Transverse Mercator Projection (WGS84; Zone 45). A volume with dimensions of $48 \times 48 \times 14\,\mathrm{km}^3$ was selected for the tomography.

Seismic data

The data set consisted altogether of 10 108 shots fired along 18 major profile lines at 60 s shot intervals corresponding roughly to a shot spacing of 150 m. In total, 23 ocean bottom hydrophones (OBH) (Flueh & Bialas 1996) recorded the shots. The sampling rate of the OBHs was 200 Hz. The drift of the OBS clocks is less than 5 ms per week and therefore negligible compared with the pick uncertainty (see below). Further details on the airgun sources and the OBH receivers can be found in, for example, Grevemeyer *et al.* (2001). Using the shot positions and the drop points of the receivers as determined by GPS, record sections of all profiles were constructed for each OBH. The receiver positions were further adjusted such that the theoretical and observed water wave arrivals matched. Data processing included an automatic gain control with 800 ms window length and a bandpass filter passing frequencies between 5 and 25 Hz and rejecting frequencies below 2 Hz and above 35 Hz. To further enhance the signal energy, a dynamic signal-noise-filter was used (Canales 1984), which down-weights noise-contaminated parts of the signal in the Fourier domain.

The general quality of the data is very good with clear arrivals seen to distances of more than 40 km (Fig. 2). Data from two OBHs and from two circular profiles around the NERO site were excluded because of timing or positioning problems. From OBHs 79 and 80 in the SE quadrant of the survey area, only data from the NW–SE profile could be used. The resulting network of 16 profiles and 21 OBHs is shown in Fig. 1.

The large data set required an automatic picking procedure for the first arrivals (Fig. 2). A time-offset window was predefined within which the first arrival was detected using a threshold criterion. The resulting traveltime curves still included many outliers depending on the signal quality. A median-despiking operator (Bednar 1983) removed most of these outliers and produced a smooth traveltime curve. Visual inspection of all picked record sections and manual editing or picking where necessary concluded the picking procedure.

Water wave arrivals were excluded by using only picks with offsets larger than the critical distance $d_c = h \tan i_c$, where h is the depth of the OBH and the critical angle $i_c = \arcsin(v_1/v_2)$, with an assumed P-wave velocity $v_1 = 1.5\,\mathrm{km\,s^{-1}}$ in water and $v_2 = 1.7\,\mathrm{km\,s^{-1}}$ in sediment (Grevemeyer *et al.* 1999), respectively. The critical distance varied from 3.1 km for the shallowest OBH to 4.0 km for the deepest OBH. A pick uncertainty had to be defined for each traveltime picked. From the inspection of the results of the automatic picking, we estimated an error of approximately 70 ms independent of the offset. Those parts of the traveltime curves with extremely poor signal-to-noise ratio were either assigned a larger error of up to 150 ms or excluded.

Altogether, the data set that served as input for the 3-D tomography consists of 68 580 traveltime observations of refracted waves recorded by 21 receivers (Fig. 1).

Bathymetry

Parallel to the seismic survey, the bathymetry of the area around the NERO site was investigated with the HYDROSWEEP system of the *R/V Sonne*. A detailed map is shown in Flueh & Reichert (1998). In order to create a bathymetric surface for the 3-D tomography, we used the water depth at each shot location as determined by the central beam of the HYDROSWEEP system and interpolated these profile-based data on to a regular grid (bin size of $400 \times 400\,\mathrm{m}^2$), which is identical to the study area of the 3-D tomography (Fig. 1). The interpolation was accomplished using continuous curvature splines in tension (Smith & Wessel 1990) as implemented in the Generic Mapping Tools (Wessel & Smith 1991, 1995). The resulting bathymetric map is shown in Fig. 3(a).

The water depth in the survey area varies between 1.63 and 2.38 km. The NERO site is located on a central high of elliptical shape with a water depth of approximately 1.7 km. Most OBHs were deployed in water depths of 1.80–1.95 km.

Magnetic data

During the 3-D seismic survey around the NERO site, a marine proton precession magnetometer towed astern of the ship on a 250 m marine cable recorded the Earth's total magnetic field intensity (Flueh & Reichert 1998). For marine surveys in remote areas, a reference station recording transient variations of the Earth's magnetic field was not available. Therefore, a correction for transient variations is difficult. Synthetic *Sq* variations for the time of the survey show amplitudes of approximately 10 nT, D_{st} indices indicate variations of up to 25 nT. The rms misfit at line intersections is of the order of 20 nT. These figures have to be compared with the size of the magnetic anomalies of interest, reaching amplitudes in excess of 300 nT. In addition, comparison of the magnetic signals of adjacent survey tracks and of repeated measurements along one

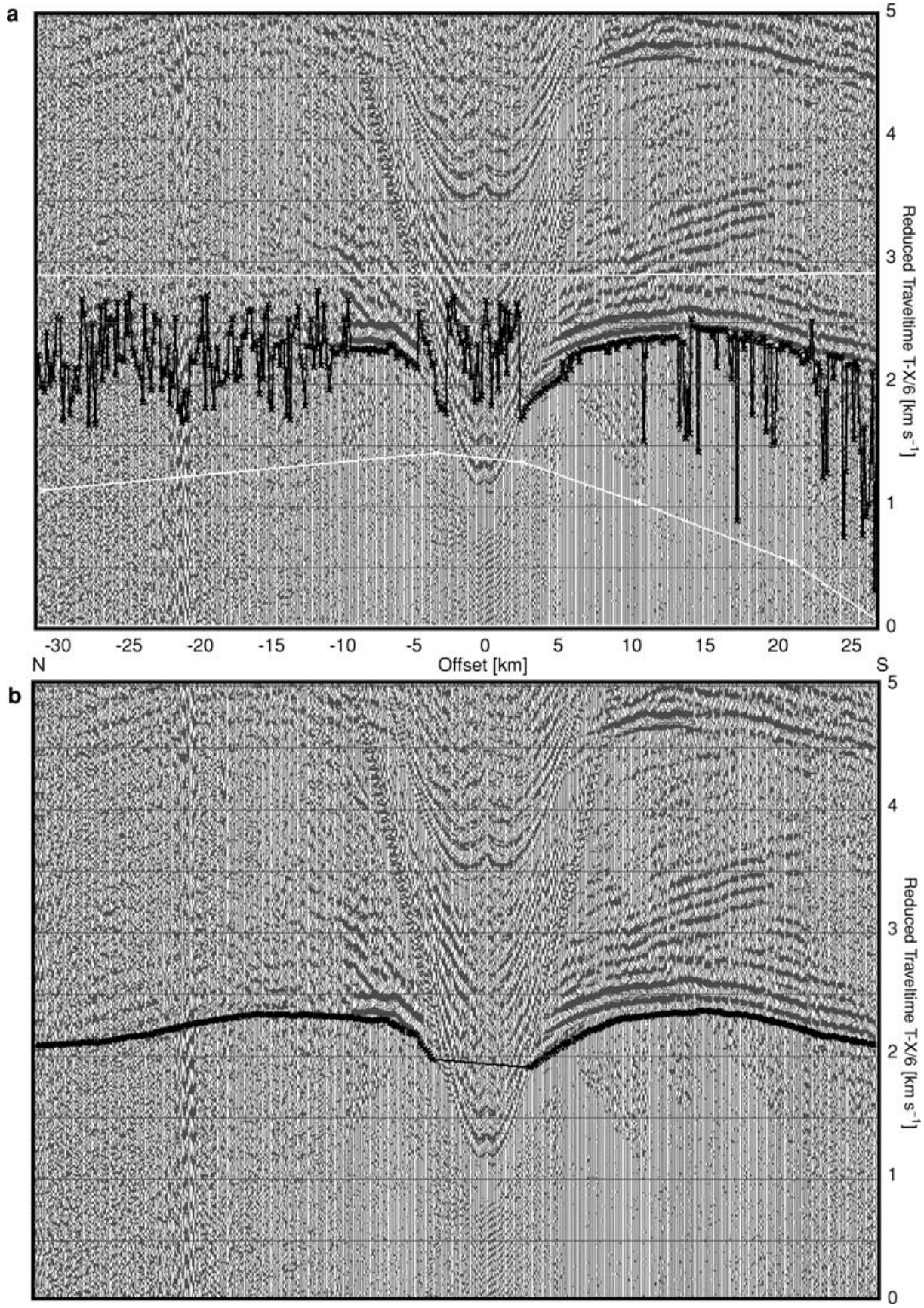

Figure 2. Data example of the N–S profile along $X = 12$ km recorded by OBH 71. The signal is enhanced by dynamic signal-noise filtering. (a) Performance of the automatic picking (black line) within the selected time window (white lines). (b) First arrivals (bold line) after median despiking and manual editing.

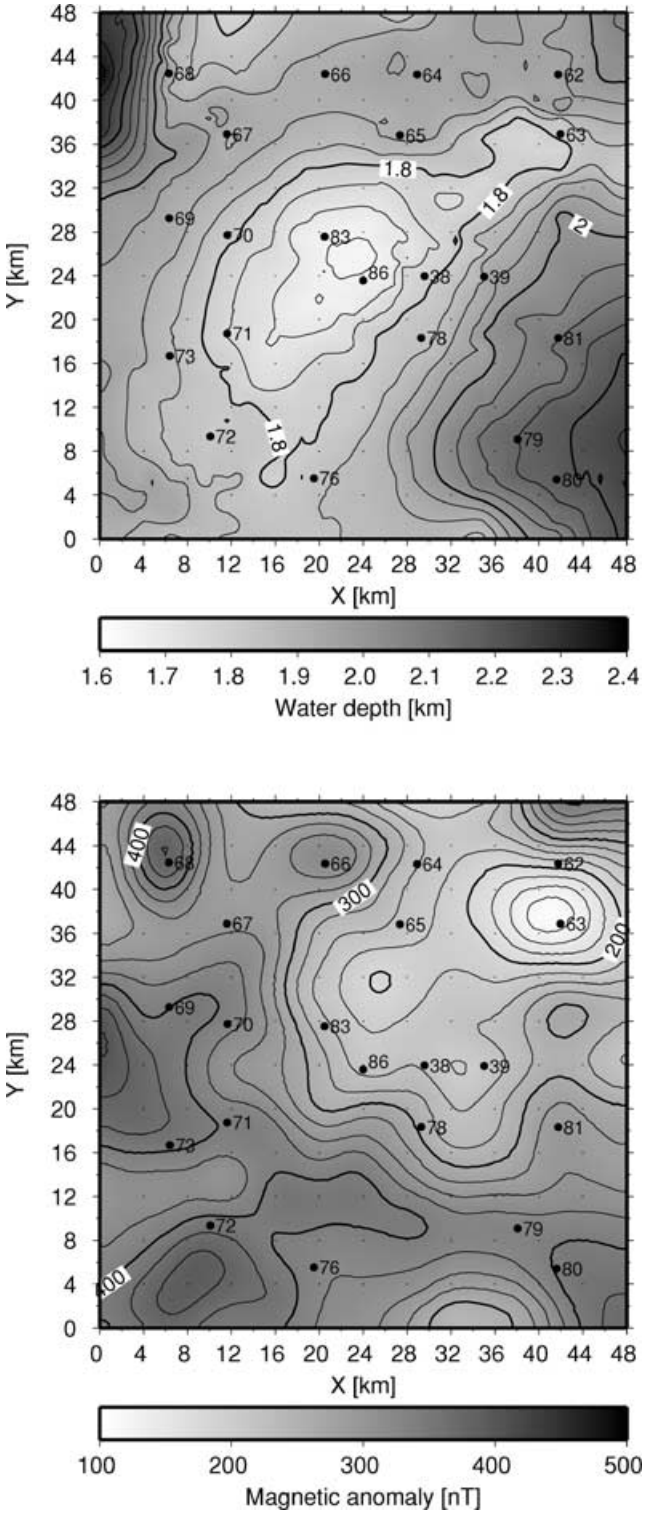

Figure 3. Map of the bathymetry of the survey area (contour interval 50 m) and the total field magnetic anomaly (contour interval 25 nT). The positions of the OBHs (solid dots) are marked and labelled.

profile segment clearly revealed the regional magnetic anomalies caused by crustal magnetization (Flueh & Reichert 1998). Therefore, the residual magnetic field was calculated simply by removing the International Geomagnetic Reference Field (IGRF). The data were gridded using continuous curvature splines in tension (Smith & Wessel 1990). Finally, a median filter with a radius 750 m was applied to the grid to reduce noise and suppress local anomalies caused by transient variations (Flueh & Reichert 1998) (Fig. 3b).

The main features of interest on the magnetic anomaly map are a positive anomaly of approximately 450 nT in the northwestern part of the survey area near OBH 68 at the intersection of three profile lines. In addition, a magnetic low with a minimum intensity of approximately 125 nT is situated in the northeastern part of the area. It is hosted in a WSW–ENE-trending magnetically 'flat' area delineated by the 225 nT contour. Comparison with the bathymetric map (Fig. 3a) indicates that both features do not correlate with or result from bathymetric highs or lows.

TOMOGRAPHY METHOD

Algorithm and choice of parameters

3-D seismic refraction surveys are becoming increasingly popular. Although tomographic methods are widely used in seismology, only a few techniques for inverting suitable seismic refraction data sets for 3-D velocity structure have been developed and tested. Zelt & Barton (1998) summarized several approaches (Hammer *et al.* 1994; Toomey *et al.* 1994; Zelt *et al.* 1996). In their study, they extensively compared two common techniques, namely regularized inversion (Toomey *et al.* 1994) and backprojection (Hole 1992), and discussed advantages and drawbacks of each method. Zelt & Barton (1998) describe a software package called FAST (First Arrival Seismic Tomography), which performs regularized inversion of a 2-D or 3-D seismic refraction data set for minimum structure. They presented the application of their 3-D tomography algorithm to a marine 3-D seismic refraction survey of the Faeroe Basin that resembles both in dimensions of the survey area and experimental setup the 3-D refraction survey of the NERO site. We therefore followed their methodology in this study to reveal the 3-D structure of the upper crust and to yield an additional example of the potential of 3-D seismic refraction surveys.

Zelt & Barton (1998) used a modified version of an algorithm presented by Vidale (1990) that forward-calculates traveltimes of first arrivals on a uniform node-based grid. The eikonal equation is solved by finite differencing. The algorithm is modified to handle large velocity gradients or contrasts encountered in upper crustal studies (Hole & Zelt 1995).

Regularized inversion not only finds a model that explains the observed traveltimes, but it also requires the solution to fulfil additional constraints, here a combination of minimum model roughness, i.e. the second spatial derivative of the model, and a small model perturbation. Several free parameters have to be defined. The parameter λ determines the trade-off between achieving a minimum data residual and a smooth model. During the inversion procedure, the maximum λ will be determined in an iterative process that produces a root mean square data residual equal to the root mean square of the pick uncertainty. Hence, the smoothest model is sought that fits the observed traveltime data within the pick uncertainty. The parameter s_z determines the relative importance of vertical versus horizontal smoothness. A suitable value for s_z was selected by trial and error (see below). The parameter α defines the relative weight of finding the smoothest (1) or least-perturbed (0) model. A value of $\alpha = 0.9$ emphasizing a smooth model was selected. The inversion algorithm of Zelt & Barton (1998) has several options to modify the inversion constraints; for example, depth-dependent weighting of the constraint parameters. The parameter choice used here is independent of depth. Finally, the parameters for the inversion include a parameter preventing edge effects. We used the value

recommended by Zelt & Barton (1998). Different values were tested and showed little effect on the solution.

The inversion is performed on a cell-based grid with uniform cell sizes that may, however, differ in x, y and z directions. The node-based forward grid has a node spacing of 0.4 km in x, y and z directions resulting in $121 \times 121 \times 36 = 527\,076$ nodes to be timed by the ray tracing algorithm. The cell-based grid for the inversion has cell sizes of $1.2 \times 1.2 \times 0.4$ km^3, resulting in $40 \times 40 \times 36 = 57\,600$ cells.

Incorporating the bathymetry

To incorporate the water layer into the model, the bathymetry served as an interface above which the model is not changed. A problem arises from the discretization of the model as a grid with a vertical node spacing of 400 m. The seismic velocities of all grid nodes nearest to the bathymetric surface and above will be held fixed at the value of the starting model (Zelt & Barton 1998). A smoothly varying bathymetry cannot be represented in this way, but the seafloor in the model is discretized in 400 m steps. The position of the seafloor in the model with respect to an OBH residing in reality at the seafloor can be incorrect by a maximum of 200 m. The problem is dealt with by timing the $5 \times 5 \times 5$ nodes surrounding the OBH using a straight ray approximation with water velocity above the OBH and an average sediment velocity below the OBH. For the upper 1 km of the crust we calculated an average velocity of 2.22 km s^{-1} using the velocities obtained from the shallow refraction study of Grevemeyer *et al.* (1999). The discretization problem will also occur where seismic rays propagating from the source at sea level penetrate into the seafloor. For example, seafloor at a depth of 1.81 km will be put in the model at the 2.0 km depth node. Hence, the seismic rays in the model will travel through 0.19 km of water with a velocity of 1.5 km s^{-1} instead 0.19 km of shallow sedimentary units with an average velocity of 1.7 km s^{-1} (Grevemeyer *et al.* 1999). This results in a traveltime delay of 15 ms. An equivalent traveltime advance arises for seafloor at 1.79 km depth, which will be positioned in the model at the 1.6 km depth node. Hence, the rays will travel erroneously through sediment with a velocity of 1.7 km s^{-1} in the model instead of water. The error caused by the discretization of the bathymetry therefore amounts to a maximum of approximately ± 15 ms, which seems negligible compared with the pick uncertainty.

Construction of a starting model

The choice of an appropriate starting model is crucial for the inversion (Zelt & Barton 1998). The assumption of linearization is only valid for small perturbations relative to a starting model, which therefore has to be close to the final model. The philosophy of 3-D tomographic images is to show velocity variations relative to a simple 1-D background or starting model. This 1-D model, for example, largely controls the depth penetration of the seismic rays.

A priori information on the seismic structure existed for a 550 km long seismic refraction profile from the Indian Basin into the Wharton Basin (Grevemeyer *et al.* 2001) cross-secting the survey area in an E–W direction and from a local refraction profile around the NERO site revealing the shallow structure (Grevemeyer *et al.* 1999). An upper sedimentary layer with seismic *P* velocities of 1.5–1.6 km s^{-1} varying in thickness from 0 to 200 m is underlain by a second unit consisting of volcaniclastic material with velocities of 2.2–3.0 km s^{-1}. The contact to the volcanic basement with velocities of 4.0–5.5 km s^{-1} is situated at approximately 400 m depth below the seafloor. The seismic velocities increase rapidly to approximately 6.0–6.3 km s^{-1} at 5–6 km depth below sea level, where the velocity gradient decreases and velocities increase more slowly, reaching 7.0 km s^{-1} at 9–12 km depth.

Table 1. Preferred starting model.

Depth range [km]	*P*-wave velocity [km s^{-1}]	Rocktype (Grevemeyer *et al.* 1999, 2001)
1.6–2.4	1.5–3.0	sedimentary layer
2.4–5.6	3.8–6.0	extrusive layer
5.6–11.0	6.15–7.0	intrusive layer

A first starting model was constructed from this information. The model was then adapted by forward modelling to match an average traveltime curve calculated by averaging all observed traveltime data in 500 m offset bins (Fig. 4). The preliminary starting model selected is a compromise between slightly higher velocities suggested by the previous seismic surveys and lower velocities required by the traveltime data. However, the shape of the traveltime curve is well matched (Fig. 4).

The next step involved a sequence of 3-D tomographic inversions all using the preliminary starting model as a background model, but different values for the parameter s_z. During each inversion run, five values for λ are tested. The model that yields a fit closest to $\chi^2 = 1$ is selected and the inversion procedure is restarted using this new model and its λ value as the new starting parameter. In this way, a final model with $\chi^2 = 1$ and maximum λ is usually found after four or five iterations. Eight such iterative inversion runs were performed with s_z values ranging from 0.05 to 0.6. The horizontal velocity variation of the resulting 3-D models is very similar and average 1-D models calculated from these 3-D velocity models barely differ. Compared with the preliminary starting model, the models require lower velocities and a less sharp change in gradient at approximately 5–6 km depth. The fit of calculated and observed average traveltimes is improved relative to the preliminary starting model (Fig. 4). Hence, the crustal structure appears vertically smooth without velocity discontinuities calling for values of $s_z \gg 0$. However, on this qualitative basis, a selection of the parameter s_z was difficult. Zelt & Barton (1998) use a minimum of the overall model perturbation and a minimum of horizontal roughness as one selection criterion for s_z. Here, the smoothest and least-perturbed model is achieved for a value of s_z of 0.4, which will therefore be used for all subsequent modelling.

The 1-D averaged model obtained from the inversion run using the preliminary starting model and $s_z = 0.4$ served as the preferred starting model for the final inversion (Fig. 4, Table 1). This model is sufficiently close to the final solution and not biased, requiring for example decreased velocities throughout all layers.

An additional test of different starting models resulted in similar horizontal velocity variations but in a different vertical velocity pattern as rays are being carried to different depth levels owing to different velocity gradients. Although the differences between the alternative 1-D starting models tested were not very large, the comparison of the average calculated and observed traveltime curves showed considerable deviations. None of these alternative starting models attained a better fit to the average observed traveltime curve than the preferred starting model. Therefore, these models were discarded.

VELOCITY STRUCTURE OF THE FINAL MODEL

Figs 5(a) and 6(a) show the velocity perturbation of the final model with respect to the preferred starting model in horizontal and vertical

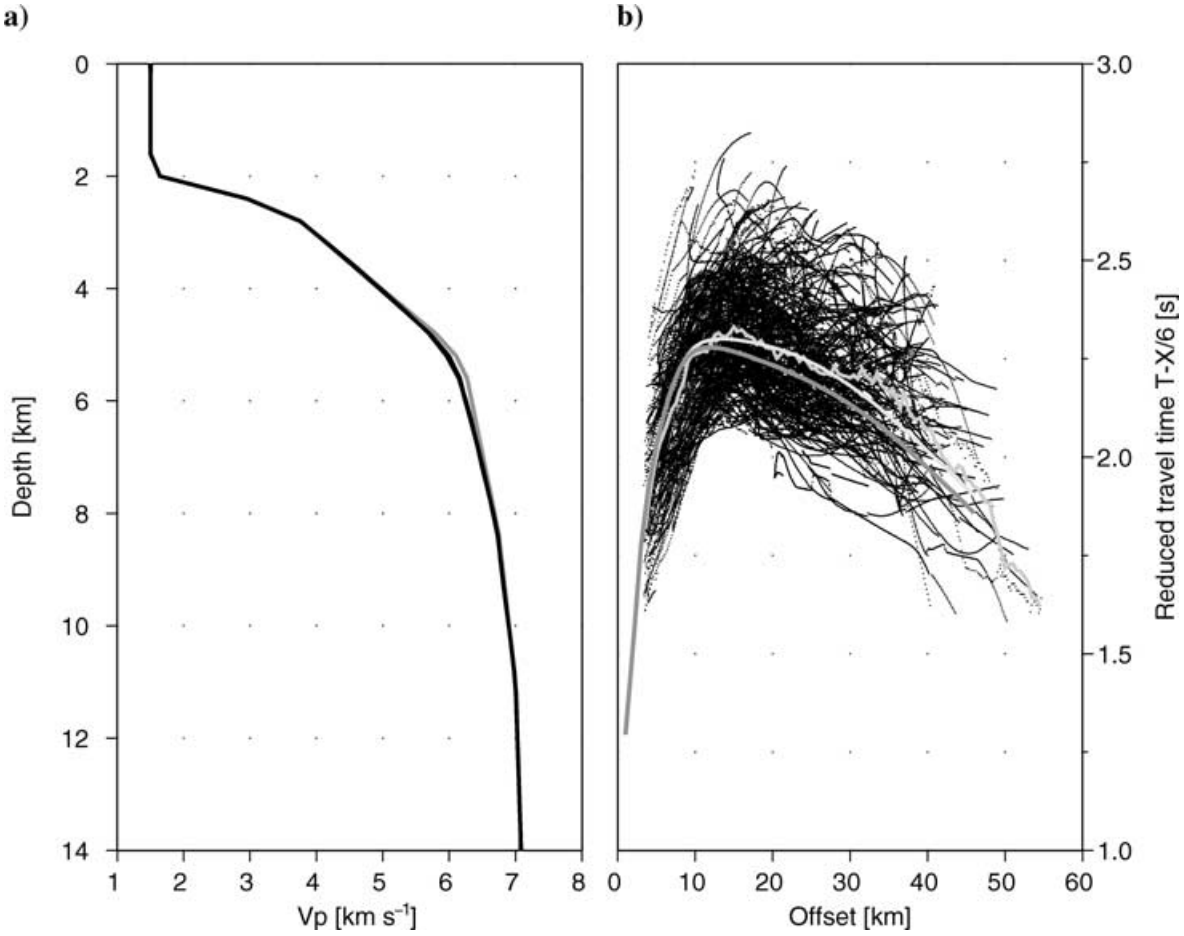

Figure 4. Construction of a starting model. (a) 1-D velocity models: preliminary starting model (grey) and preferred starting model obtained from inversion using the preliminary starting model and parameter $s_z = 0.4$ (black). (b) Complete set of observed traveltimes (dots). The spiky grey line represents the averaged traveltime curve of all data in 500 m bins. It is almost matched by the calculated traveltime curve of the preliminary 1-D starting model (dark grey). The fit is improved for the preferred starting model (light grey).

cross-sections, respectively. Regions not sampled by seismic rays are not shown. Fig. 6(b) shows absolute seismic velocities on vertical cross-sections.

The most striking feature of the horizontal velocity cross-sections (Fig. 5a) is the prominent region of low velocities in the southeastern part of the survey area. It extends down to at least 8 km depth, reaching its maximum perturbation amplitudes of approximately -0.6 km s^{-1} at 5 km depth. This low-velocity area is bounded to the north by a SW–NE-striking plateau-like structure with increased seismic velocities. Below 5 km depth, the low-velocity structure extends further north, resulting in a clear separation of a seismically fast western half of the survey area and a seismically slow eastern half of the survey area.

The vertical cross-sections (Fig. 6a) further illustrate the east–west separation of the seismic structure in the southern part of the survey area. North of 30 km, a slow eastern half and a fast western half persist only at depths below 5 km, whereas an area of increased velocities is situated in the shallow northeastern part of the crustal block. A prominent feature is the channel of increased seismic velocities in the cross-section at 42 km. It extends well down into the crust, reaching velocity perturbations of up to 0.4 km s^{-1}. This anomaly appears in the horizontal cross-sections as a small-scale circular anomaly around OBH 68.

The contrasts in seismic velocities are more difficult to see in the plots of absolute seismic velocities (Fig. 6b). Here, only the most dominant features are evident: a trough of low velocities in the southeastern part of the survey area with the 6.0 km s^{-1} contour line reaching down to 6 km depth in contrast to a 5 km depth elsewhere. The channel of high-seismic velocities at $X = 5$ km and $Y = 42$ km shows up with upward bending of all contour lines.

RESOLUTION TESTS

Before any of these structures can be interpreted geologically, extensive tests of the resolution of the model and its reliability have to be performed.

Traveltime residuals

Fig. 7 compares the traveltime residuals of the preferred starting model and the final model. A significant reduction of the residuals could be achieved. The symmetrical shape of the histograms about a residual of zero further indicates that the starting and final model are not biased.

The root mean square residuals for most stations are 70 ms or less. OBH 68 yields a large residual of 83 ms. Thus, the high-velocity anomaly beneath this station could even be more pronounced to account for the observed traveltime curve of this station. This,

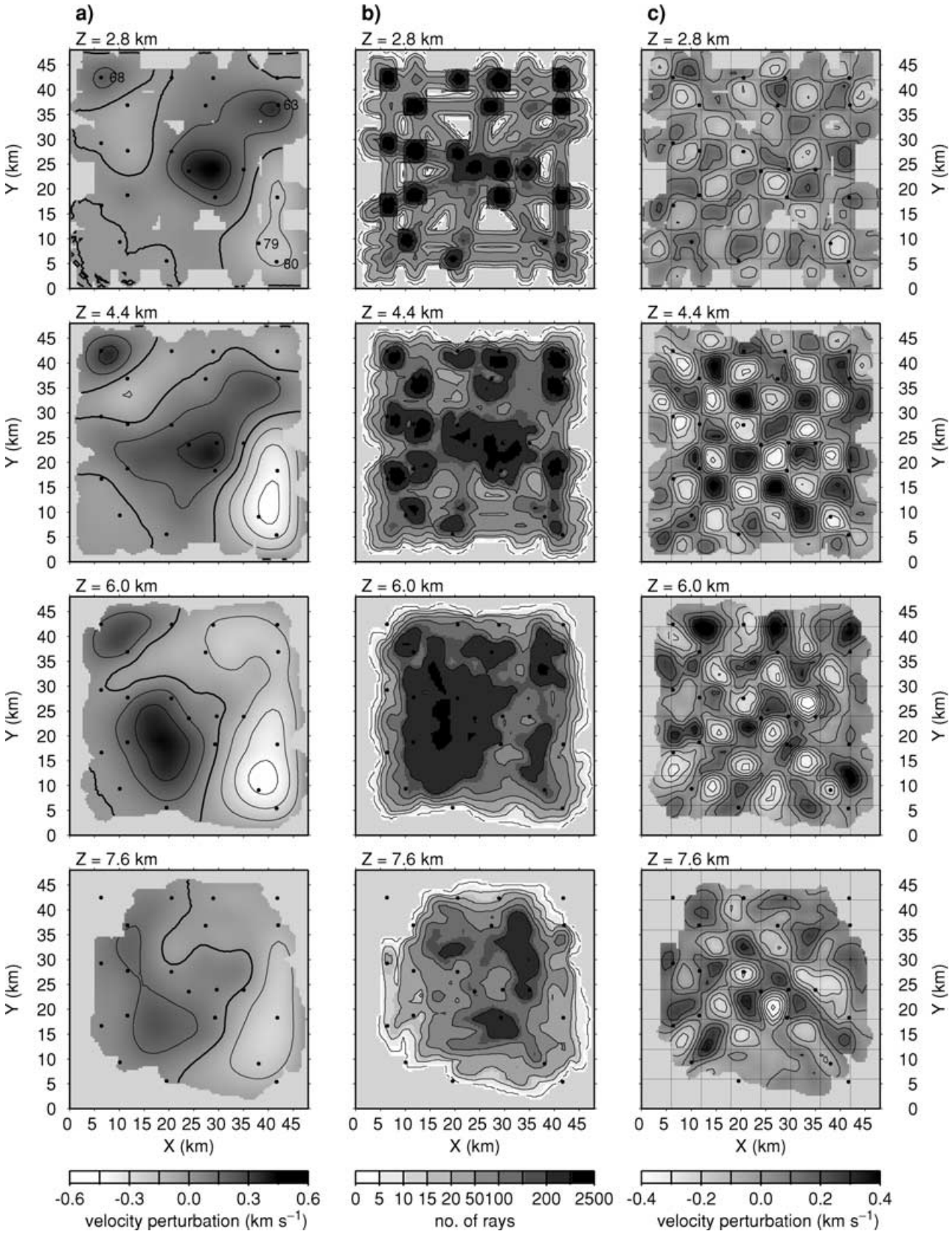

Figure 5. Horizontal cross-sections through the final velocity model at depths below sea level as indicated. (a) Velocity perturbation relative to the preferred starting model (Fig. 4) (contour interval, 0.15 km s^{-1}; bold line, zero perturbation). Dots mark OBH positions in all slices. OBHs referred to in the text are labelled. Grey areas are not sampled by rays. (b) Ray coverage of final model (contours: 2,10, 20, 50, 100 and 200 rays). (c) Chequerboard test. The recovered pattern from an original chequerboard pattern with 6 × 6 km^2 alternating positive and negative velocity anomalies of 0.2 km s^{-1} (grid lines) is shown (contour interval, 0.1 km s^{-1}).

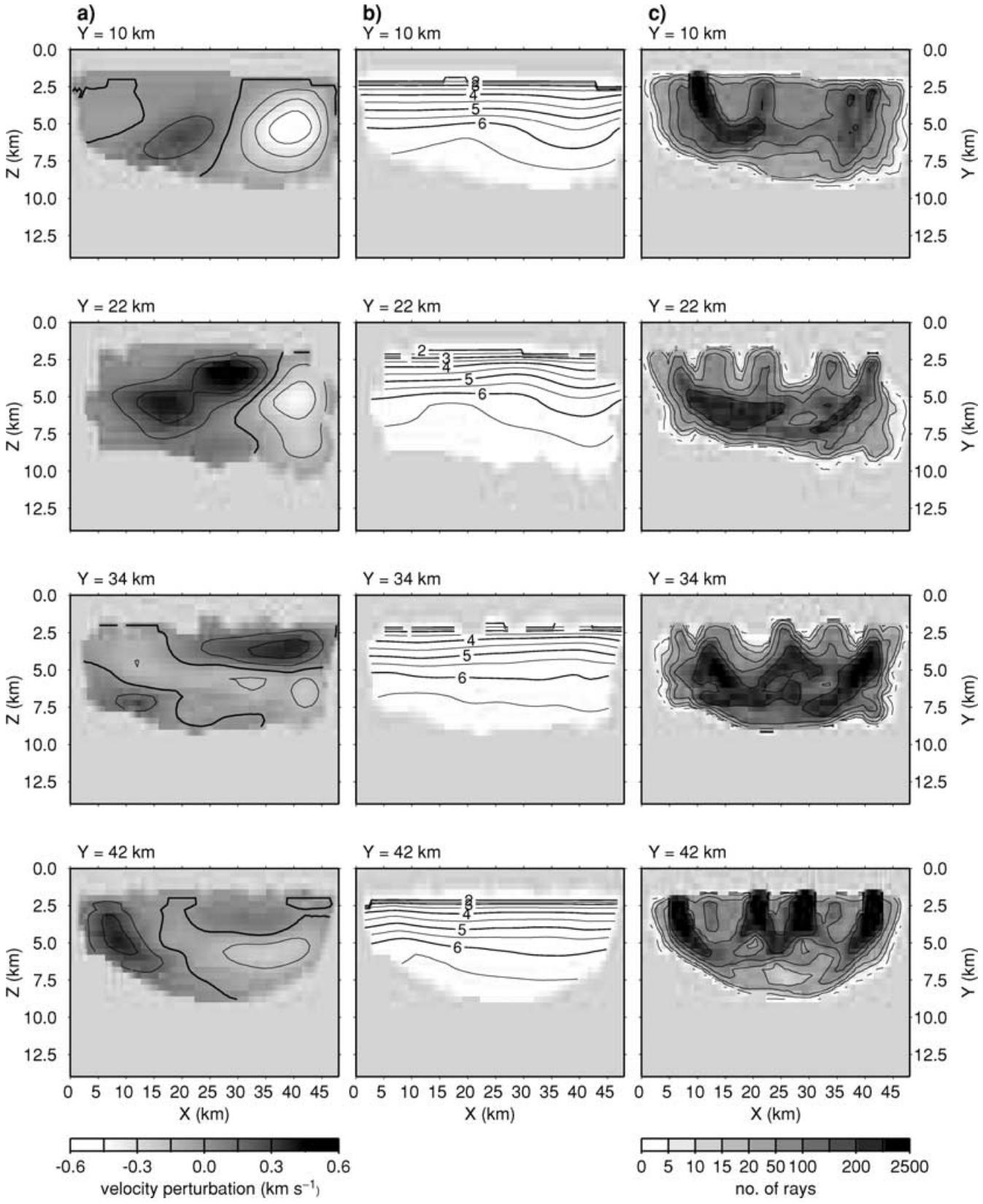

Figure 6. Vertical E–W cross-sections through the final model at *Y* positions as indicated. (a) Velocity perturbation relative to the preferred starting model (Fig. 4) (contour interval, 0.15 km s^{-1}; bold line, zero perturbation). Grey areas are not sampled by rays. (b) Absolute seismic velocities (contour interval, 0.5 km s^{-1}) (c) Ray coverage of the final model (contours as in Fig. 5b).

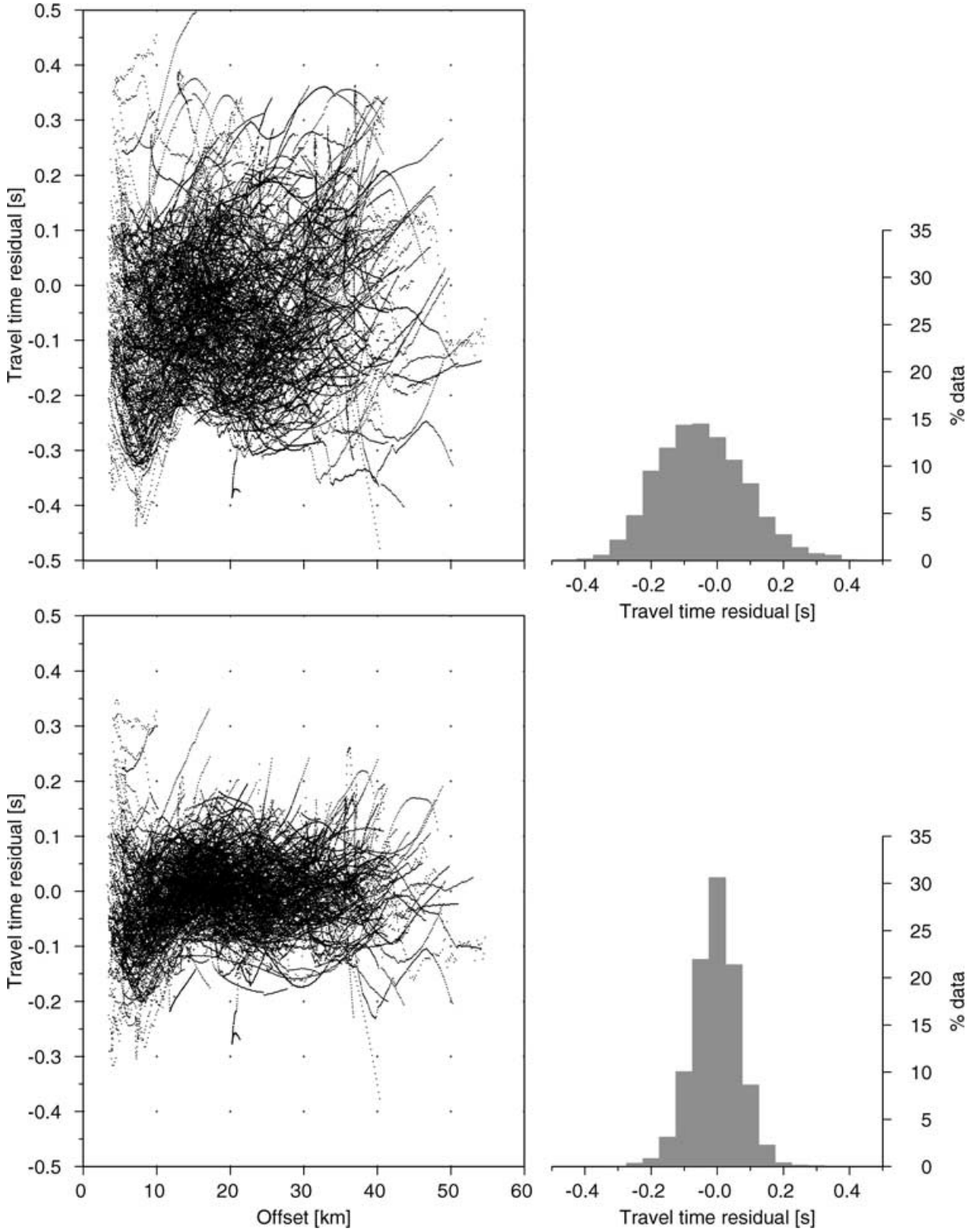

Figure 7. Traveltime residuals of the preferred starting model (above) and the final model (below). The residuals are calculated as observed minus calculated traveltimes. The histograms give the percentage of residual values in 0.05 s bins. The residuals are distributed symmetrically about 0 indicating that the models are not biased.

however, is prevented by the smoothness constraint of the inversion. A similar problem arises for OBHs 79 and 80. The traveltime curves show significant residuals for small offsets calling for lower velocities in the uppermost crust. As the few near-offset rays observed at OBHs 79 and 80 are the only rays with turning points in the uppermost crust in that area, the inversion tolerates the few large traveltime residuals in order to keep the model smooth. Insufficient representation of the shallow structure in the model involves the risk

that shallow-velocity anomalies are carried to larger depths along the ray paths of distant *P*-wave arrivals. Therefore, additional tests were needed to verify the existence of the pronounced low-velocity anomaly underneath OBHs 79 and 80 (see the discussion below).

Ray coverage

A first impression of the reliability of the resulting 3-D velocity model is gained by plotting the number of rays traversing each cell (Figs 5b and 6c). In the shallow part of the crust, areas of high ray coverage concentrate around the OBH sites from which rays depart near-vertically, sampling the immediately adjacent cells intensively. However, vertical propagation of rays does not yield direct information on the seismic velocities in this area. Rays with turning points, i.e. horizontal propagation, are needed. A limited number of rays sample these shallow depths along the profile lines with sparse ray coverage in the SE quadrant. From 4 to 7 km depth, the model is well sampled. The vertical cross-sections in Fig. 6(c) show that many rays have their turning points at these depths. Below 7 km, the ray coverage becomes poorer. The central area of the model can be considered as sufficiently well sampled down to approximately 8.5 km depth. As expected, the ray coverage decreases towards the model edges at all depths. Therefore, features such as the eastward termination of the prominent low-velocity anomaly (Figs 5a , 6a and b) have to be interpreted with caution.

Chequerboard test

The ability of a 3-D seismic refraction experiment to resolve lateral velocity variations can be analysed in a chequerboard test (Zelt 1998; Zelt & Barton 1998). The chequerboard model used here consists of alternating positive and negative velocity anomalies of 0.2 km s^{-1} amplitude and horizontal dimensions of 6×6 km^2. This chequerboard pattern is the same at all depths. It is superimposed on the preferred 1-D starting model. Synthetic traveltimes were calculated for this chequerboard model and a random error of ± 70 ms added. This data set was then inverted using the same parameters as for the final inversion of the observed traveltime data. Fig. 5(c) shows the recovered chequerboard pattern. The alternating squares with reduced and increased seismic velocity are clearly discernible from 2.8 to approximately 6 km depth. The pattern is less well recovered at the margins of the area sampled by seismic rays. This becomes particularly evident below 6 km depth, where lateral velocity variations of 6 km size can only be resolved in the central part of the survey area. The amplitude of the recovered chequerboard pattern is lower than the original pattern at shallow depth and is larger at greater depth.

INTERPRETATION AND DISCUSSION

Crustal structure

The 3-D tomography imaged the crust down to approximately 6 km below the seafloor. This depth penetration is not sufficient to gain a complete impression of the crustal architecture of the survey area. However, an interpretation appears promising within the context of previous studies. Grevemeyer *et al.* (2001) attributed seismic velocities of 3.3–5.5 km s^{-1} to mainly extrusive rocks, underlain by intrusive rocks with velocities of 6.5–7.2 km s^{-1}. A prominent decrease in vertical velocity gradient marks the transition from predominantly extrusive to intrusive rocks at approximately 3–4 km depth beneath the seafloor in the Ninetyeast Ridge volcanic edifice. Seismic velocities of the extrusive complex are thought to be lower than in the adjacent oceanic basins, probably caused by the higher porosity of lava flows extruding from volcanic centres situated near the sea level (Peirce *et al.* 1989) and the presence of volcaniclastic material. Grevemeyer *et al.* (2001) consider the upper 10 km of the crust as part of the volcanic edifice built up by hotspot volcanism on to the pre-existing oceanic crust.

Referring to this interpretation, the 3-D tomography mainly yields an image of the structure of the volcanic edifice. The depth of the transition from extrusive to intrusive rocks is roughly delineated by the 6 km s^{-1} isovelocity line in Fig. 6(b). In agreement with the results of Grevemeyer *et al.* (2001), this transition is located at 5–6 km depth or 3–4 km below the seafloor.

Comparison of the final velocity model with charts of bathymetry (Fig. 8a), magnetic anomalies (Fig. 8b) and preliminary isochron maps of the thickness of the sedimentary cover (Flueh & Reichert 1998) gives additional confidence in the details of the final velocity model and provides important constraints for the geological interpretation.

The prominent low-velocity anomaly is delineated nicely by the 2000 m isobath as seen in Fig. 8(a): a bathymetric low occupies the same area as the seismic anomaly. The plateau in the centre of the survey area correlates to some extent with predominantly high-seismic velocities down to approximately 4 km depth, especially the northeastern extension of the plateau (Fig. 8a). The circular high-velocity anomaly in the NW corner of the survey area, in contrast, is situated at the edge of a slope without any remarkable bathymetric expression.

The shallow-velocity structure (Fig. 5a, $Z = 2.8$ km) is only well resolved at short offsets around the OBHs. However, the horizontal velocity variation closely resembles a map of the thickness of the sedimentary cover derived from near vertical seismic data recorded along the shooting lines (Flueh & Reichert 1998). A sediment layer thinner than the starting model appears as a positive velocity perturbation, a thicker layer as a negative perturbation: basement outcrops are seen close to OBHs 68 and 63 (Flueh & Reichert 1998), represented in our model by increased seismic velocities. The sedimentary cover is also thin on the elevated area SE of the NERO site as correctly reflected in the tomography model. The low-velocity anomaly in the SE quadrant of the survey area coincides with a sedimentary cover of up to 700 m compared with 200–400 m elsewhere (Flueh & Reichert 1998). However, owing to poor ray coverage and the model smoothness constraint, the velocity perturbations in the shallow crust of the final model reach a maximum peak-to-peak amplitude of only approximately 0.4 km s^{-1}, which is considerably lower than the pronounced velocity contrast between outcropping basement rock ($v_p > 3.8$ km s^{-1}) and sedimentary rocks ($v_p = 1.6$–3.0 km s^{-1}). This is reflected by large residuals of OBHs 68, 79 and 80 situated in anomalous regions at the margins of the model where the ray coverage is particularly poor.

We also tested relaxed smoothness and perturbation constraints for the velocity nodes at 1.6–2.8 km depth. The traveltime residuals for OBHs 68, 79 and 80 decreased and the amplitudes of the velocity anomalies in this depth range increased, whereas the interpretable general structure remained unaffected. The depth range with relaxed inversion constraints contained fine-scale structure that cannot be resolved by our survey design. We therefore preferred to use uniform inversion constraints for all depths for the final inversion (Figs 5 and 6) and emphasize the limitations of this final model.

In addition, we performed an inversion using a starting model that explicitly includes an additional 400 m of sediment in the SE

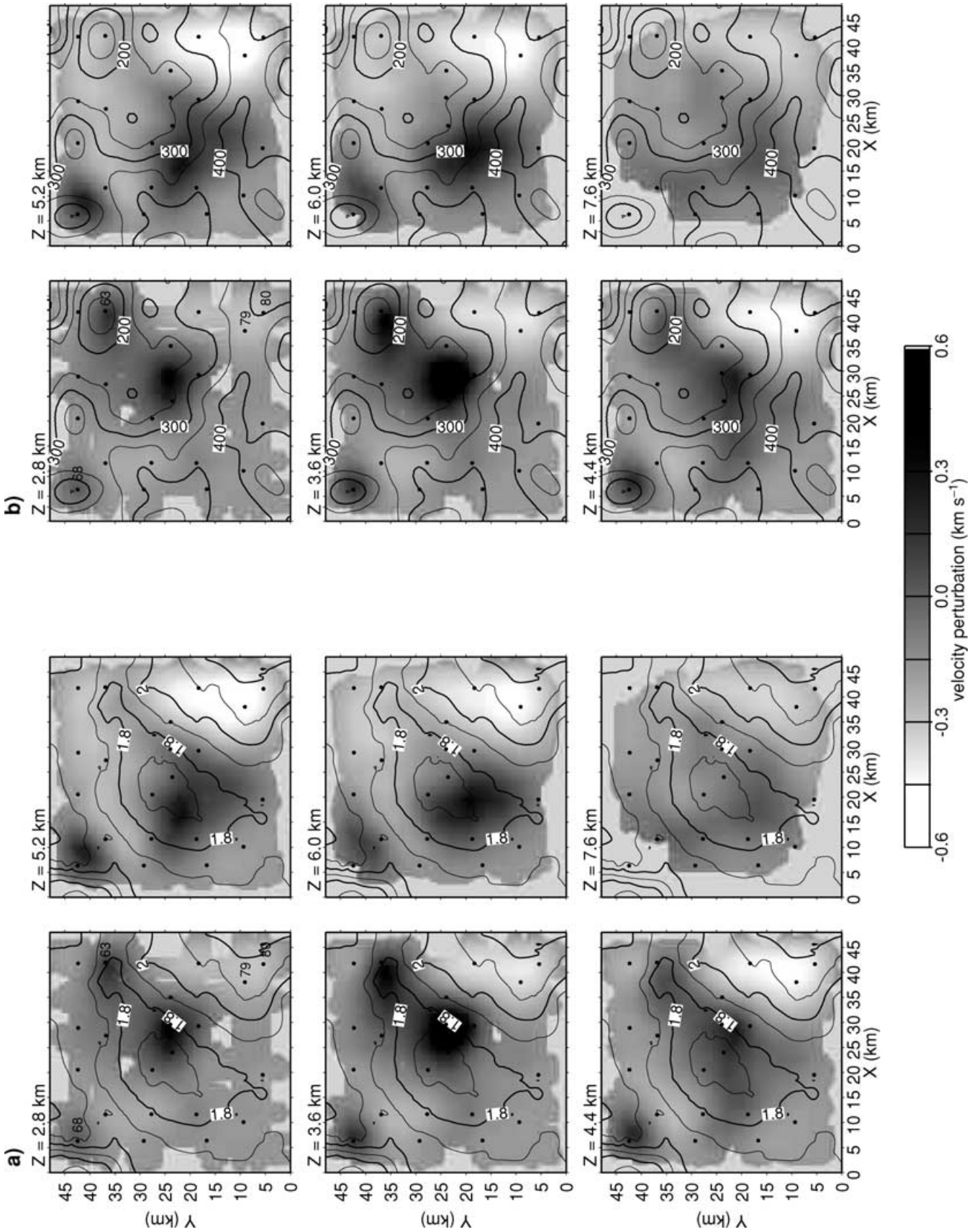

Figure 8. Comparison of the horizontal velocity variations (grey shading) of the final model (Fig. 5a) and (a) the bathymetry of the survey area (contour interval, 100 m) and (b) the magnetic anomalies (contour interval, 50 nT). The depth below sea level of the horizontal sections is indicated. OBHs referred to in the text are labelled.

quadrant of the survey area in order to test whether the pronounced low-velocity anomaly at greater depth might be an artefact resulting from insufficient representation of the sedimentary layer in the final model. The maximum amplitude of the anomaly decreased from 0.6 to 0.45 km s^{-1} and the traveltime misfit of OBHs 79 and 80 was considerably improved but not removed. The same test with 800 m of additional sediment overcompensated the effect of the sedimentary basin. The low-velocity anomaly was reduced to approximately 0.15 km s^{-1}, but traveltimes of near-offset rays clearly indicated seismic velocities that were too low in the shallow crust. We therefore concluded that the low-velocity anomaly beneath the sedimentary basin in the SE quadrant of the model is a real feature; however, its amplitude is increased by smearing the poorly resolved shallow low-velocity anomaly to a larger depth. The same applies to the high-velocity anomaly beneath OBH 68.

Fig. 8(b) compares the positions of seismic and magnetic anomalies. A striking feature is the coincidence of the high-velocity anomaly beneath OBH 68 with a local magnetic high of approximately the same lateral dimensions as the seismic anomaly. This observation further supports the reliability of the 3-D seismic tomography model, weakening any arguments that a local velocity anomaly underneath a single OBH might not be trustworthy. In addition, the northeastern part of the survey area shows a domain of high-seismic velocities in the upper 4 km of the model that correlates with a magnetically 'flat' area of comparably low-magnetic intensities that is delineated by the 250 nT contour and also comprises the local minimum of the magnetic field near OBH 63. Below 4 km depth, this correlation is lost. The low-velocity anomaly in the southeastern part of the survey area has no magnetic expression.

The correlation of seismic and magnetic anomalies may point to crustal material that has formed over a relatively short time period to acquire a uniform magnetization and seismic properties different from adjacent areas. The anomaly beneath OBH 68 might represent remnants of a volcanic centre extending down into the upper crust with high-velocity intrusive rocks of uniform (positive) magnetization. The extended shallow high-velocity anomaly coinciding with lower magnetic field values than the surrounding area could eventually stem from a massive lava flow that cooled rapidly, preferably during a reversed polarity epoch of the Earth's magnetic field. The source of this lava flow might be near OBH 63, where outcrops of the volcanic basement are reported and the magnetic anomaly shows the lowest values. The low-velocity trough in the southeastern part of the survey area, in contrast, might represent an unsorted accumulation of extrusive material of different polarities that produces no significant magnetic anomaly. In this area, the transition to predominantly intrusive material is located approximately 1 km deeper than in the remaining survey area, suggesting an increased thickness of the extrusive sequence. One might speculate that the anomaly represents a pre-existing topographic depression that filled with extrusives and volcaniclastic material. The bathymetric data may further support this hypothesis. The nearly linear, sharp southeastern edge of the central plateau seems to result from failure of the southeastern flank of the plateau. A large volcanic avalanche occurred that deposited large amounts of volcaniclastic material at the foot of the flank where a thick sedimentary sequence and anomalously low-seismic velocities are observed by the seismic studies. Small volcanic cones representing late-stage volcanism (Kopf *et al.* 2001) are found to reside above the deposits of the volcanic avalanche, suggesting an earlier origin of the avalanche.

Kopf *et al.* (2001) describe a number of small cones several 100 m in diameter and approximately 200 m high that were located by a multibeam sonar study on the eastern slope of the central plateau in the area between OBH 63 and 39 (Fig. 1). Several lines of our survey traverse the field of volcanic cones. However, the structures seem to be too localized to produce any detectable seismic or magnetic anomalies. Kopf *et al.* (2001) interpreted these cones as representing centres of late-stage volcanism post-dating the main activity by approximately 5 Myr. Lava flow from these centres is thought to have occurred towards the east, away from the already existing central plateau as indicated by the increasing thickness of volcanic deposits towards the east. This implies that the presumed massive lava flow that builds up the elongated ridge at the northeastern end of the central plateau as demonstrated by coincident magnetic and seismic anomalies clearly stems from an earlier period of more voluminous volcanic activity. This age constraint may also apply to the fossil volcanic centre in the northwestern part of the survey area. The dimensions of the volcanic centre and its seismic and magnetic properties are distinctly different from the volcanic cones described by Kopf *et al.* (2001). Furthermore, such late-stage volcanic cones are not seen on the central plateau nor in the area to the northwest, where the fossil volcanic centre is situated (Kopf *et al.* 2001). It is more difficult to establish a relationship between the volcanic centre in the northwest and the lava flow at the northeastern extension of the plateau. The different polarities of the magnetic anomalies point to a formation at different times. The resolution of the 3-D tomography at depths below 7 km and its ability to determine the depth extent of the seismic anomaly beneath OBH 68 are too restricted to detect, for example, a common feeder system.

CONCLUSIONS

The 3-D tomography of the extrusive upper crust of the Ninetyeast Ridge at approximately 17°S provided useful information in various aspects: a comprehensive seismic model of the crust beneath the NERO site can now be established: an approximately 160 m thick layer of pelagic sediments with velocities of 1.5–1.6 km s^{-1} is underlain by a layer of volcaniclastic material with 2.2–3.0 km s^{-1} (Flueh & Reichert 1998; Grevemeyer *et al.* 1999). The transition to volcanic basement occurs at 400–700 m depth below the seafloor (Flueh & Reichert 1998). Velocities rapidly increase from approximately 3.5 to 6.2 km s^{-1} at 5–6 km depth below the seafloor. Our study revealed in detail the heterogeneous structure and varying thickness of this layer (interpreted as being extrusive upper crust). A prominent decrease in vertical velocity gradient marks the transition from mainly extrusive to intrusive rocks at approximately 5–6 km depth or 3–4 km below the seafloor in agreement with the results of the 550 km long refraction profile of Grevemeyer *et al.* (2001). The intrusive layer extends deeper than the maximum penetration of the 3-D tomography. Grevemeyer *et al.* (2001) studied the deep crustal structure: they report velocities of approximately 7.2 km s^{-1} at the base of the intrusive layer in 18 km depth. Geologically this layer consists of the intrusive part of the volcanic edifice and the pre-hotspot oceanic crust. However, the seismic properties of these units are too similar to make a distinction. The crust–mantle transition is situated at approximately 24 km depth beneath a layer with seismic velocities of 7.5–7.6 km s^{-1}, interpreted as magmatic underplate (Grevemeyer *et al.* 2001).

In the extrusive layer of the crust, three types of volcanic features could be identified by their distinct seismic, magnetic and bathymetric nature.

(1) A fossil volcanic centre characterized by a narrow-seismic high-velocity anomaly, a positive magnetic anomaly, but no

particular bathymetric expression. The depth extent of the structure is difficult to constrain with our data.

(2) A thick lava flow showing up as increased seismic velocities down to 4 km depth and a pronounced magnetic low. The area forms the northeastern elongation of an elevated plateau. An outcropping basement and the largest magnetic anomaly values might point to the source of the lava sequence in the area of OBH 63.

(3) Small volcanic cones, manifesting late-stage volcanism (Kopf *et al.* 2001), which do not produce seismic or magnetic anomalies detectable by our survey setup.

Apart from insights into the volcanic structure of the upper crust, the results of our 3-D seismic refraction tomography will contribute to a comprehensive understanding of earthquake signals to be recorded by the future permanent seismic observatory NERO. The detailed knowledge of the seismic structure of the underlying crust will allow one to predict traveltime anomalies relative to a standard Earth model that arise from the 3-D structure of the crust. This will guarantee that full advantage of this remote observatory can be taken.

ACKNOWLEDGMENTS

We thank C.A. Zelt and V. Sallares for their thorough reviews that helped to clarify the text. The data used in this study were acquired and pre-processed with funds from the German Federal Ministry of Education and Research (BMBF), grant nos 03G0131A and 03G0131B; this is gratefully acknowledged.

REFERENCES

Bednar, J.B., 1983. Applications of median filtering to deconvolution pulse estimation and statistical editing of seismic data, *Geophysics,* **48,** 1598–1610.

Canales, L.L., 1984. Random noise reduction, *Annual Meeting Abstracts,* Society of Exploration Geophysicists.

Duncan, R.A., 1991. Age distribution of volcanism along aseismic ridges in the eastern Indian ocean, *Proc. ODP Init. Rep.,* **121,** 507–517.

Flueh, E.R. & Bialas, J., 1996. A digital, high data capacity ocean bottom recorder for seismic investigations, *Int. Underwater Syst. Design,* **18,** 18–20.

Flueh, E.R. & Reichert, C., eds., 1998. Cruise Report SO131, SINUS—seismic investigations at the Ninetyeast Ridge observatory using SONNE and JOIDES RESOLUTION during ODP Leg 179, *GEOMAR report,* **72,** 337.

Flueh, E.R., Grevemeyer, I. & Reichert, C., 1999. Investigating the crustal framework at the NERO Hole 1107A, Leg 179, *JOIDES J.,* **25,** 14–16.

Grevemeyer, I. & Flueh, E.R., 2000. Crustal underplating and its implications for subsidence and state of isostasy along the Ninetyeast Ridge hotspot trail, *Geophys. J. Int.* **142,** 643–649.

Grevemeyer, I., Flueh, E.R., Herber, R. & Villinger, H., 1999. Constraints on the shallow seismic structure at Ocean Drilling Program Site 1107, Ninetyeast Ridge, from implosive bottom sources and airgun shots, *Geophys. Res. Lett.,* **26,** 907–910.

Grevemeyer, I., Flueh, E.R., Reichert, C., Bialas, J., Kläschen, D. & Kopp, C., 2001. Crustal architecture and deep structure of the Ninetyeast Ridge hotspot trail from active-source ocean bottom seismology, *Geophys. J. Int.* **144,** 414–431.

Hammer, P.T.C., Dorman, L.M., Hildebrand, J.A. & Cornuelle, B.D., 1994. Jasper Seamount structure: seafloor seismic refraction tomography, *J. geophys. Res.,* **99,** 6731–6752.

Hole, J.A., 1992. Nonlinear high-resolution three-dimensional seismic travel time tomography, *J. geophys. Res.,* **97,** 6553–6562.

Hole, J.A. & Zelt, B.C., 1995. Three-dimensional finite-difference reflection travel times, *Geophys. J. Int.* **121,** 427–434.

Kopf, A., Klaeschen, D., Weinrebe, W., Flueh, E.R. & Grevemeyer, I., 2001. Geophysical evidence for late stage magmatism at the central Ninetyeast Ridge, Eastern Indian Ocean, *Mar. Geophys. Res.,* **22,** 225–234.

Montagner, J.P., Karczewski, J.F. & Romanowicz, B., 1994. A first step toward an oceanic geophysical observatory, *EOS, Trans. Am. geophys. Un.,* **75,** 150–154.

Peirce, J.W., 1978. The northwards motion of India since the Late Cretaceous, *Geophys. J. R. astr. Soc.,* **52,** 277–312.

Peirce, J.W. *et al.*, 1989. *Proc. ODP init. Rep.,* **121,** Ocean Drilling Program, College Station, TX.

Royer, J.-Y., Peirce, J.W. & Weissel, J.K., 1991. Tectonic constraints on the hotspot formation of the Ninetyeast Ridge, *Proc. ODP Sci. Res.,* **121,** 763–776.

Smith, W.H.F. & Wessel, P., 1990. Gridding with continuous curvature splines in tension, *Geophysics,* **55,** 293–305.

Toomey, D.R., Solomon, S.C. & Purdy, G.M., 1994. Tomographic imaging of the shallow crustal structure of the East Pacific Rise at 9°30′N, *J. geophys. Res.,* **99,** 24 135–24 157.

Vidale, J.E., 1990. Finite-difference calculation of travel times in three dimensions, *Geophysics,* **55,** 521–526.

Wessel, P. & Smith, W.H.F., 1991. Free software helps map and display data, *EOS, Trans. Am. geophys. Un.,* **72,** 441.

Wessel, P. & Smith, W.H.F., 1995. New version of the Generic Mapping Tools released, *EOS, Trans. Am. geophys. Un.,* **76,** 329.

Zelt, C.A., 1998. Lateral velocity resolution from three-dimensional seismic refraction data, *Geophys. J. Int.* **135,** 1101–1112.

Zelt, C.A. & Barton, P.J., 1998. Three-dimensional seismic refraction tomography: a comparison of two methods applied to data from the Faeroe Basin, *J. geophys. Res.,* **103,** 7187–7210.

Zelt, B.C., Ellis, R.M., Clowes, R.M. & Hole, J.A., 1996. Inversion of three-dimensional wide-angle seismic data from the southwestern Canadian Cordillera, *J. geophys. Res.,* **101,** 8503–8529.